MATERIALS CHEMISTRY FRONTIERS

RESEARCH ARTICLE

View Article Online
View Journal | View Issue

Cite this: *Mater. Chem. Front.*, 2023, **7**, 3657

Multifunctional nanomicelles constructed *via* an aggregation and de-aggregation strategy for magnetic resonance/NIR II fluorescence imaging-guided type I photodynamic therapy†

Lirong Wang,‡[ab] Ji Qi,‡[d] Ke Zhang,[e] Zeyan Zhuang,[ab] Keke Ding,[f] Xu Chen,[ab] Hong Shan,[e] Dan Ding,[d] Anjun Qin *[ab] and Ben Zhong Tang[bcg]

Received 4th April 2023,
Accepted 16th May 2023

DOI: 10.1039/d3qm00347g

rsc.li/frontiers-materials

Fluorescence and magnetic resonance imaging (FL/MRI) has received much attention due to their complementary characteristics. However, the simultaneous enhancement of fluorescence and MR signals plus the efficacy of the treatment is still a major challenge. To tackle this difficulty, we put forward a strategy of aggregation and de-aggregation based on luminogens with aggregation-induced emission (AIE) features. NIR II photosensitizer 4,4′-(6,7-diphenyl-[1,2,5]thiadiazolo[3,4-*g*]quinoxaline-4,9-diyl)bis(*N*,*N*-diphenylaniline) (TQ-TPA) with type I reactive oxygen species (ROS) generation ability and amphiphilic 2TPE-Gd were synthesized, and both of them showed the AIE feature. During the construction of nanomicelles, hydrophobic TQ-TPA spontaneously aggregated into the core of the nanomicelles formed by 1,2-distearoyl-*sn*-glycerol-3-phosphoethanolamine-*N*-methoxy(polyethylene glycol)-2000 (DSPE-PEG). Meanwhile, aggregates of 2TPE (tetraphenylethylene)-Gd in aqueous solution could be de-aggregated and inserted into the interface, and formed TGdTT nanomicelles (NMs). Based on this strategy and the AIE feature, the TGdTT NMs exhibited strong NIR II fluorescence and type I ROS generation ability, and enhanced T_1 relaxivity (r_1). Moreover, *in vitro*, *in vivo*, and pharmacokinetics results demonstrated that these nanomicelles have good biosafety and a long blood circulation time. Finally, they allowed successful realization of complementary MR/NIR II fluorescence dual-modal imaging-guided photodynamic therapy (PDT) to inhibit tumor growth. This work demonstrated that the aggregation and de-aggregation strategy of AIEgens in core–shell nanomicelles is very attractive for constructing multifunctional theranostic probes.

1. Introduction

The combination of diagnostics and therapeutics, that is, theranostics, is a trend in clinical practice in fighting against cancer because it provides real-time feedback of treatment and holds great potential in enhancing the accuracy of diagnosis and improving the efficacy of therapy. For a diagnostic system, multi-modal imaging guarantees accurate determination of tumor location at an early stage,[1–3] for which the most popular combination is fluorescence imaging and magnetic resonance imaging (FLI/MRI) because of their complementary characteristics.[4,5] MRI has the merits of high tissue penetration depth and spatial resolution, but has low sensitivity. This disadvantage could be remedied by FLI. However, the low light penetration of fluorescence probes limits their further applications. Recently, NIR II organic fluorophores have received increased attention because of their higher biosafety than inorganic ones, and deeper penetration depth and higher signal-to-noise ratio than red- or NIR-FLI.[6–10] Therefore, how to integrate these fluorophores with MRI contrast agents (CAs) to realize effective and multifunctional

[a] *State Key Laboratory of Luminescent Materials and Devices, Guangdong Provincial Key Laboratory of Luminescence from Molecular Aggregates, South China University of Technology, Guangzhou 510640, China. E-mail: msqinaj@scut.edu.cn*
[b] *Center for Aggregation-Induced Emission, AIE Institute, South China University of Technology, Guangzhou 510640, China*
[c] *School of Science and Engineering, Shenzhen Institute of Aggregate Science and Engineering, The Chinese University of Hong Kong, Shenzhen, 518172, Guangdong, China*
[d] *State Key Laboratory of Medicinal Chemical Biology, College of Life Sciences, Nankai University, Tianjin 300071, China*
[e] *Center for Interventional Medicine, The Fifth Affiliated Hospital, Sun Yat-sen University, Zhuhai 519000, China*
[f] *Department of Urology, The First Affiliated Hospital of Soochow University, Suzhou 215006, China*
[g] *Hong Kong Branch of Chinese National Engineering Research Centre for Tissue Restoration and Reconstruction, The Hong Kong University of Science & Technology, Clear Water Bay, Kowloon, Hong Kong, China*

† Electronic supplementary information (ESI) available: The synthesis scheme of 2TPE-Gd, Fig. S1–S25, measurement of PL quantum yields, ROS detection, T_1 relaxivity. See DOI: https://doi.org/10.1039/d3qm00347g

‡ These authors contributed equally to this work.

theranostic effects has become a hot and challenging topic for researchers. In general, the conjugation of a fluorescent probe with an MRI CA, such as Magnevist® (Gd-diethylenetriamine-penta-acetic acid (DTPA)) or Dotarem® (Gd-tetra-azacyclo-dodecatetraacetic acid (DOTA)), could realize dual-modal FLI/MRI.[11–14] However, in most cases, the fluorescence intensity of conventional fluorophores can be easily quenched by the gadolinium complexes due to the heavy-atom effect[11] or aggregation-caused quenching (ACQ) effect.[15]

In contrast, aggregation-induced emission luminogens (AIEgens) exhibit brighter emission in their aggregated states than in solution because of the restriction of intramolecular motion (RIM), providing them with tremendous advantages, such as high fluorescence quantum yields, anti-photobleaching effects, and long-term tracing for *in vivo* imaging.[16,17] In addition, some AIEgens bearing a strong electron donor (D) and acceptor (A) could serve as photosensitizers (PSs) to simultaneously enhance fluorescence and ROS generation ability.[18,19] Among the AIE PSs, the ones that mostly generate type I ROS (H_2O_2, $O_2^{\bullet-}$, $^{\bullet}OH$, *etc.*) have attracted tremendous attention owing to their stronger hypoxia tolerance than traditional PSs that mainly generate type II ROS ($^1O_2$),[20–23] and are excellent alternative materials for photodynamic therapy (PDT).[24] Therefore, conjugating AIEgens with Gd-based CAs to form AIE-Gd probes would be an ideal way to construct dual-modal imaging and therapeutic agents. The aggregation of AIEgens could not only enhance the fluorescence intensity, but also the large size of the AIE-Gd aggregates could prolong the rotational correlation time (τ_R)[25,26] to improve the T_1 relaxivity (r_1). However, AIE-Gd aggregates generally show enhanced emission upon aggregation in aqueous solution due to amphipathic properties, but their r_1 usually only improves slightly.[27] This could be attributed to the tight aggregation of AIE-Gd hindering the accessibility of Gd to water molecules in the bulk solution, although they have larger size than when non-aggregated, thus leading to the low efficiency in improving r_1. These results suggest that simply aggregating amphipathic AIE-Gd molecules is not an effective strategy for enhancing their MRI performance. Controlling their aggregation in a loose structure for the diffusion of water molecules, which could increase the accessibility of slowly diffusing water molecules to Gd,[28–30] would be a strategy to simultaneously enhance the fluorescence intensity and r_1.

Tetraphenylethylene (TPE) is a typical AIE molecule and has been commonly utilized to design new AIEgens. In 2011, Tang's group reported that aggregates of amphiphilic TPE derivatives could be easily de-aggregated by the incorporation of enough surfactant, resulting in weakened emission.[31] This de-aggregation could form micelles with TPE derivatives interspersed in their shells. As is known, nanomicelles (NMs) are a good nano-delivery system and have received widespread attention in biomedical fields because of their facile preparation, large loading capacity, and good biocompatibility, making them highly translatable for biomedical applications.[32] Moreover, the interior and interface of NMs can be loaded with different functional molecules, according to their hydrophilicity and hydrophobicity, for theranostics.[33,34] This inspired us to utilize a surfactant to load different multifunctional AIEgens. Based on differences in hydrophilicity, the surfactant would be dispersed in the core and shell of micelles respectively through aggregation and de-aggregation processes. Herein, we firstly synthesized a hydrophobic molecule, 4,4′-(6,7-diphenyl-[1,2,5]thiadiazolo[3,4-*g*]quinoxaline-4,9-diyl)bis(*N*,*N*-diphenylaniline) (TQ-TPA), and an amphipathic molecule, 2TPE-Gd-DOTA (2TPE-Gd), both of which showed AIE feature. Then, 1,2-distearoyl-*sn*-glycerol-3-phosphoethanolamine-*N*-methoxy(polyethylene glycol)-2000 (DSPE-PEG) was chosen for loading these two molecules, with a feeding-weight ratio of 16 : 16 : 1 (TQ-TPA : DSPE-PEG : 2TPE-Gd) to form NMs (named as TGdTT NMs), which realized the improvement of r_1 by keeping these two molecules dispersed in the interface and core of the NMs, respectively (Fig. 1). As expected, these multifunctional TGdTT NMs have a spherical morphology with a size of 52.2 ± 10.2 nm, exhibiting NIR absorption, NIR II emission, and good type I ROS generation ability. Meanwhile, the r_1 of the TGdTT NMs showed a 5-fold increment compared with that of the clinical MRI CA Gd-DOTA. Accordingly, TGdTT NMs with good biocompatibility and biosafety realized MR/NIR II FL dual-modal imaging both *in vitro* and *in vivo* and effective type I ROS generation for cancer-cell killing and tumor inhibition. All these results confirmed that our designed TGdTT NMs would be a good type I PS for MR/NIR II FL imaging-guided PDT.

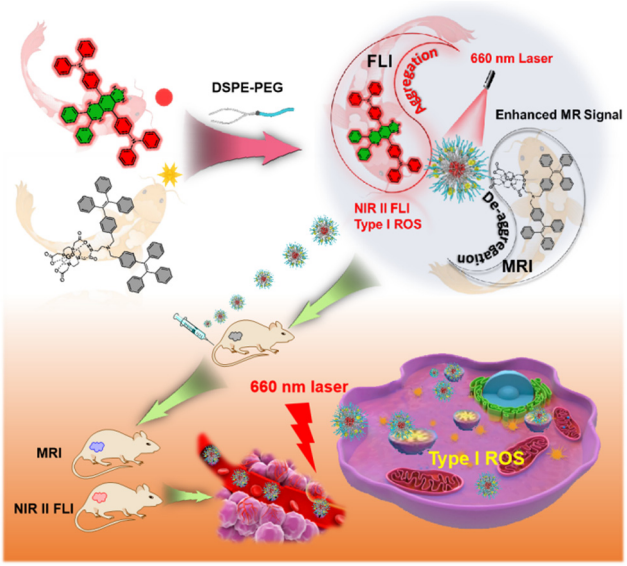

Fig. 1 Schematic illustration of the construction of TGdTT NMs and their application in MR/NIR II FL dual-modal imaging-guided type I photodynamic therapy.

2. Experimental

2.1 Materials

All chemicals, unless otherwise noted, were purchased from commercial sources and used without further purification. $GdCl_3$ was purchased from Alfa Aesar. 1,4,7,10-Tetra-azacyclododecane (min. 98% CYCLEN) was purchased from Strem Chemicals, Inc. Bromotriphenylethylene and 4-bromo-*N*,*N*-diphenylaniline were obtained from Soochiral Chemical Science &

Technology Co., Ltd. *N*-Bromosuccinimide was purchased from J&K Scientific, Ltd. 4-Tolylboronic acid was obtained from Alfa Aesar. Azobisisobutyronitrile (AIBN), potassium carbonate (K_2CO_3) and magnesium sulfate ($MgSO_4$) were purchased from Aladdin Co., Ltd. Tetrakis(triphenylphosphine)palladium ($Pd(PPh_3)_4$) was obtained from Energy Co., Ltd. Ultra-filtration units (Amicon® Ultra 15 mL filters with 30 kDa nominal molecular-weight cutoff) were purchased from Merck Millipore Corp.

2.2. Synthesis of *N*,*N*-diphenyl-4-(tributylstannyl)aniline (2)

4-Bromo-*N*,*N*-diphenylaniline (**1**, 4.86 g, 15 mmol) was added into a 250 mL Schlenk flask. The flask was then evacuated and purged with dry nitrogen three times, and anhydrous THF (80 mL) was added. Then the mixture was cooled to −78 °C, and maintained at this temperature for 15 min, followed by the addition of *n*-butyllithium (*n*-BuLi, 2.5 M hexane solution, 6 mL, 15 mmol). After stirring at this temperature for 2 h, tri-*n*-butyltin chloride (4.6 mL, 17 mmol) was added, and the mixture was slowly warmed to room temperature, and stirred overnight. Then water was added to quench the reaction, and the mixture was extracted with DCM three times. The organic phases were combined and dried over anhydrous $MgSO_4$. After removal of the solvent under reduced pressure, the crude product (**2**) was used for the next reaction without further purification. ^{1}H NMR (400 MHz, $CDCl_3$, 25 °C) δ (ppm): 7.31 (t, 2H), 7.24 (t, 4H), 7.09 (d, 4H), 7.05–6.97 (m, 4H), 1.60–1.51 (m, 6H), 1.36–1.27 (m, 6H), 1.12–1.09 (m, 6H), 0.98 (t, 9H).

2.3. Synthesis of 4,4′-(5,6-dinitrobenzo[*c*][1,2,5]thiadiazole-4,7-diyl)bis(*N*,*N*-diphenylaniline) (4)

N,*N*-Diphenyl-4-(tributylstannyl)aniline (**2**, 6.4 g, 12 mmol), 4,7-dibromo-5,6-dinitrobenzo[*c*][1,2,5]thiadiazole (**3**, 1.92 g, 5 mmol), and $Pd(PPh_3)_4$ (335 mg, 0.3 mmol) were added to a 250 mL two-necked round-bottom flask. The flask was then evacuated and purged with dry nitrogen three times, and anhydrous THF (150 mL) was added. The mixture was refluxed for 24 h. After cooling down to room temperature, water was added to quench the reaction, and the mixture was washed with DCM three times. The organic phases were combined and dried over $MgSO_4$, and the solvent was evaporated under reduced pressure. The crude product was purified by silica gel column chromatography using dichloromethane/hexane (1 : 2 v/v) as the eluent. A dark purple solid (**4**) was obtained in 72% yield (2.56 g). ^{1}H NMR (400 MHz, CDCl3): δ 7.41(d, 4H), 7.33 (t, 8H), 7.22 (d, 8H), 7.13 (t, 8H).

2.4. Synthesis of 4,7-bis(4-(diphenylamino)phenyl)benzo[*c*][1,2,5] thiadiazole-5,6-diamine (5)

To a mixture of compound **4** (1.43 g, 2 mmol) and acetic acid (150 mL) in a 250 mL two-necked round-bottom flask, iron powder (3.36 g, 60 mmol) was added. The mixture was heated to 80 °C and stirred for 6 h. After cooling down to room temperature, water was added, and the mixture was washed with DCM three times. The organic phases were combined and dried over $MgSO_4$, and the solvent was evaporated under reduced pressure. The crude product (**5**) was used directly for the next step without further purification.

2.5. Synthesis of 4,4′-(6,7-diphenyl-[1,2,5]thiadiazolo[3,4-*g*]quinoxaline-4,9-diyl)bis(*N*,*N*-diphenylaniline) (TPA-TQ)

Compound **5** (196 mg, 0.3 mmol) and benzil (**6**, 126 mg, 0.6 mmol) were dissolved in a mixture of chloroform (20 mL) and acetic acid (20 mL) in a 100 mL flask. The reaction mixture was heated to 60 °C, and stirred for 12 h. Then water was added, and the mixture was extracted with DCM three times. The organic phases were combined and dried over anhydrous $MgSO_4$. After the removal of the solvent under reduced pressure, the residue was purified by silica gel column chromatography using DCM/hexane (1 : 2 v/v) as the eluent. A dark blue solid of TPA-TQ was obtained in 72% yield (178.7 mg,). ^{1}H NMR (400 MHz, $CDCl_3$) δ (ppm): 7.98 (d, 4H), 7.66 (d, 4H), 7.38 (d, 2H), 7.37–7.25 (m, 24H), 7.10 (t, 4H). ^{13}C NMR (100 MHz, $CDCl_3$) δ (ppm): 153.13, 152.73, 148.04, 147.55, 138.58, 136.06, 134.02, 130.08, 129.56, 129.35, 128.57, 128.22, 128.19, 125.18, 123.39, 121.61, 99.99. HRMS (MALDI-TOF) calculated for $C_{56}H_{39}N_6S$ $[M + H]^+$ *m*/*z*: 827.2957, found: 827.2954.

2.6. Synthesis of tri-*tert*-butyl 2,2′,2″-(10-(2-((2-(bis(4-(1,2,2-triphenylvinyl)benzyl)amino)ethyl)amino)-2-oxoethyl)-1,4,7,10-tetraazacyclododecane-1,4,7-triyl)triacetate (9)

Tri-*tert*-butyl-2,2′,2″-(10-(2-((2-aminoethyl)amino)-2-oxoethyl)-1,4,7,10-tetraazacyclododecane-1,4,7-triyl)triacetate (DOTA*t*Bu-NH_2) (**7**, 100 mg, 0.16 mmol) was synthesized according to previous reports.[35] It's acetonitrile solution containing Et_3N (3–5 drops) was added dropwise to the acetonitrile solution of 1,1,2-triphenyl-2-(4-bromomethylphenyl)ethylene (**8**, 135.6 mg, 0.32 mmol) and K_2CO_3 (27.6 mg, 0.2 mmol). After finishing the addition, the solution was refluxed for 1 h. After filtration and solvent evaporation, the crude product was purified by silica gel column chromatography using dichloromethane/methanol (10 : 1 v/v) as the eluent. A white powder (**9**) was obtained in 98% yield (207.9 mg). ^{1}H NMR (400 MHz, $CDCl_3$): δ 7.37 (s, 1H), 7.15–6.82 (m, 38H), 5.27 (s, 1H), 3.56 (d, 32H), 1.43 (d, 27H).^{13}C NMR (100 MHz, $CDCl_3$): δ 172.55, 171.03, 143.26, 141.85, 140.72, 137.44, 131.59, 128.34, 127.16, 126.09, 81.82, 57.24, 56.36, 55.71, 53.56, 52.90, 28.04. HRMS (MALDI-TOF) calculated for $C_{84}H_{98}N_6O_7Na$ $[M + Na]^+$ *m*/*z*: 1325.7385, found: 1325.7395.

2.7. Synthesis of compound 2TPE-Gd

Compound **9** (100 mg, 0.08 mmol) was dissolved in 5 mL trifluoroacetic acid (TFA) at room temperature. After stirring for 6 h, excess TFA was removed by rotary evaporation. The resultant white solid product was dissolved in methanol, and the pH of the solution was adjusted to 5–6 with dilute sodium hydroxide solution. Afterward, anhydrous gadolinium chloride (24 mg, 0.09 mmol) in 3 mL methanol was added dropwise to the solution. After reaction overnight at 60 °C, the methanol was removed by evaporation. The crude product was re-dissolved in DCM, and the excess gadolinium ions were washed away with water. A white solid of 2TPE-Gd was obtained in 90% yield (92.9 mg). HRMS (MALDI-TOF) calculated for $C_{72}H_{72}N_6O_7Gd$ $[M + H]^+$ *m*/*z*: 1290.4703; found: 1290.4673.

2.8. Cell Culture

Murine breast cancer 4T1 cells were cultured in Dulbecco's modified Eagle's medium (DMEM) containing 10% fetal bovine serum at 37 °C in a humidified environment containing 5% CO_2.

2.8.1. Cell colocation by confocal microscopy. 4T1 cells were seeded at a density of 2×10^4 cells per plate on a 35 mm dish. Cells were incubated with TGdTT NMs with a Gd(III) concentration of 10 μM for 4 h, and then washed twice with PBS. Fresh medium with LysoTracker™ Red (2 μM) was added and further incubated for 15 min. Then cells were washed three times with PBS and fresh medium was added for confocal fluorescence imaging using a Zeiss LSM 710 confocal laser scanning microscope. The excitation wavelength of 405 nm and emission wavelength of 410–520 nm were set for the TGdTT NMs, while those for LysoTracker™ Red were 570 nm and 590–700 nm, respectively.

2.8.2. Cell viability without laser irradiation. The cytotoxicity of the TGdTT NMs was assessed *via* the 3-(4, 5-dimethylthiazol-2-y1)-2, 5-diphenyltetrazolium bromide (MTT) assay. 4T1 cells were firstly seeded into a 96-well plate at a density of 5000 cells per well in DMEM and incubated for 24 h. Then the medium was replaced with TGdTT NMs with different Gd(III) concentrations (0, 1.56, 3.13, 6.25, 12.5, 25 and 50 μM) and the cells were incubated for an additional 24 h. After incubation, the culture medium was removed and each well was filled with 100 μL of fresh culture medium containing MTT (0.5 mg mL^{-1}) and incubated for an additional 4 h. Then, the medium was discarded and each well was filled with 100 μL DMSO. The optical density (OD)490 value (Abs.) of each well was immediately measured using a microplate reader. Cell viability was expressed by the ratio of the OD490 values of the cells incubated with the TGdTT NM suspension to that of the cells incubated with culture medium only.

2.8.3. *In vitro* MR imaging and cell uptake. 4T1 cells were seeded into three tissue-culture dishes at a density of 1×10^7 per dish. After incubation for 24 h, the medium was replaced by medium with TGdTT NMs or Gd-DOTA, both at the same Gd(III) concentration (30 μM), or PBS. The cells were washed with PBS three times and harvested into 200 μL microcentrifuge tubes. T_1-Weighted phantom images of the cells were obtained on a 0.5 T NMR120-Analyst system with the following parameters: repetition time (TR) = 100 ms and echo time (TE) = 5.3 ms. The intensities at regions of interest (ROI) were quantified using ImageJ. After imaging tests, the Gd contents of these samples were analyzed *via* inductively coupled plasma mass spectrometry (ICP-MS).

2.9. *In vivo* MRI

Animal experiments were carried out according to the protocol approved by the Institutional Animal Care and Use Committee (IACUC) of South China University of Technology. Clinical CA Gd-DOTA was used as a control. MR imaging was conducted on a 9.4 T MRI scanner. The same slices were acquired at different times (0, 1, 4, 7, and 24 h) after intravenous injection. All the images were obtained using the T1_FLASH sequence with parameters as follows: TR/TE = 300/3.0 ms. The MR contrast-to-noise ratio (CNR) was evaluated by finely analyzing the ROIs of the tumor and surrounding tissue. $CNR = |SNR_{tumor} - SNR_{tissue}|/SNR_{tissue}$ (SNR = signal-to-noise ratio). The contrast enhancement was defined as CNR_{post}/CNR_{pre}.

2.10. *In vivo* FLI

Female BALB/c mice bearing subcutaneous 4T1 tumors were intravenously injected with TGdTT NMs at a dose of 0.5 g per kg body weight. Fluorescence images were collected at indicated times (0, 1, 4, 7, and 24 h) using a full spectrum animal *in vivo* imaging system, AniView Phoenix 600 (Guangzhou Biolight Biotechnology Co., Ltd).

2.11. Pharmacokinetics

To determine the blood circulation half-lives, TGdTT NMs were intravenously injected into healthy female BALB/c mice (n = 3 per group) at a dose of 0.5 g per kg body weight. At predetermined times (10 min, 20 min, 0.5 h, 1 h, 2 h, 4 h, 8 h, 12 h, and 24 h) after injection, approximately 20 μL blood was collected from the tail. The amount of Gd(III) in these samples was measured by ICP-MS. The final amount of Gd(III) was calculated as the percentage of the injected dose per gram of tissue (% ID per g).

2.12. Biodistribution

4T1 tumor-bearing female BALB/c mice were injected with TGdTT NMs at a dose of 0.5 g per kg body weight, and were sacrificed at 4, 7 or 24 h post injection (n = 3 per group). Hearts, livers, spleens, lungs, kidneys, intestines, and tumors were collected and weighed. The amount of Gd(III) in these samples was measured using ICP-MS. The final amount of Gd(III) was calculated as the percentage of the injected dose per gram of tissue (% ID per g).

2.13. *In vivo* efficacy

A subcutaneous tumor was constructed by injecting 1×10^6 4T1 cells in the right hind leg of female BALB/c mice. After the volume of the tumor was about 50 mm^3, these tumor-bearing mice were randomly divided into four groups (n = 3 per group): PBS, only TGdTT NMs, only laser irradiation, and TGdTT NMs plus laser irradiation. In order to obtain effective tumor inhibition, the injection and laser irradiation treatment was carried out every four days. The tumor volume and body weight were measured every other day. The tumor volume was calculated according to the equation: tumor volume = (tumor length) × $(\text{tumor width})^2/2$. Relative tumor volumes were calculated as V/V_0 (V_0 is the tumor volume before treatment and V is the volume after treatment).

2.14. Biosafety assessment

Healthy female BALB/c mice (n = 3 per group) were intravenously injected with TGdTT NMs at a dose of 0.5 g per kg body weight. PBS was used as a control. After 30 days, blood samples were collected from the orbital sinus by quickly removing the eyeball from the socket with a pair of tissue forceps. Then, liver function index including alanine aminotransferase (ALT), aspartate aminotransferase (AST) and albumin (ALB), and renal

function index including creatinine (Cr), uric acid (UA) and urea (UREA) were detected. In addition, the tissues of the mice (heart, liver, spleen, lung and kidney) were collected to be sectioned and stained with hematoxylin and eosin for histological assessment.

2.15. Statistical analysis

Least-significant difference (LSD) tests were used to determine whether the variance between groups is similar. The sample size ($n = 3$) was chosen to evaluate the statistical analysis, which was performed using SPSS (IBM Corp.). Statistical significance was calculated using two-tailed LSD tests and defined as $^{*}P < 0.001$.

3. Results and discussion

3.1. Synthesis and characterization of TQ-TPA

To obtain low-bandgap AIE PSs, the D–A strategy is generally employed.[36] In this work, we chose thiadiazolo[3,4-*g*]quinoxaline (TQ) and triphenylamine (TPA) as the electron-accepting and donating moieties to build the target molecule, TQ-TPA, and its synthetic route is shown in Fig. 2A. The intermediates and target molecule were characterized by ^{1}H and ^{13}C NMR (Fig. S1–S4, ESI†). Afterwards, the photophysical properties of TQ-TPA were investigated. As expected, TQ-TPA shows an absorption peak at 630 nm and a broad emission spectrum with a peak at 917 nm and tail to 1200 nm (Fig. 2B). Moreover, the photoluminescence (PL) spectra of TQ-TPA in THF/water mixture showed that at water fraction (f_w) values of up to 60%, its emission gradually weakened due to the twisted intramolecular charge transfer (TICT) process; after that, the emission intensified because of the formation of aggregates and activation of the RIM process (Fig. S5, ESI†).

To explore the ROS generation ability of TQ-TPA, we used 2′,7′-dichlorofluorescein (DCFH) as a total ROS indicator. To make it disperse better in water, TQ-TPA was fabricated into nanomicelles by encapsulation with DSPE-PEG at a weight ratio of 1 : 1. According to the mechanism of DCFH detection, ROS can oxidize non-fluorescent DCFH to fluorescent DCF. As shown in Fig. 2C and Fig. S6 (ESI†), the fluorescence intensity of DCF incubated with 20 μM of TQ-TPA NMs exhibited a 500-fold improvement compared with that of only DCFH under 660 nm laser irradiation at a power of 0.3 W cm^{-2}. Furthermore, TQ-TPA NMs showed a concentration-dependent ROS generation ability. Even at a low concentration of 5 μM, TQ-TPA NMs exhibited a 280-fold enhancement compared with only DCFH under the same conditions. Next, we used the type I indicator hydroxyphenyl fluorescein (HPF) and type II indicator 9,10-anthracenediyl-bis(methylene)-dimalonic acid (ABDA) to identify the types of ROS. The remarkably increased PL intensity of HPF suggested that TQ-TPA mainly generated hydroxyl radicals ($^{\bullet}$OH, type I ROS) (Fig. 2D). Meanwhile, the slightly decreased absorption intensity of ABDA (Fig. 2E and Fig. S7, ESI†) suggested that singlet oxygen ($^{1}O_2$, type II ROS) was hardly generated.

To gain a detailed insight into the favorable generation of type I ROS by TQ-TPA, we carried out a theoretical study using M06-2X/6-311G(d,p) and M06-2X/def2-TZVP programs in Gaussian 16. The results indicated the highest occupied molecular orbital (HOMO) and lowest unoccupied molecular orbital (LUMO) of the optimized TQ-TPA structure in the ground state (S_0) and excited states (S_1 and T_1) are separated and distributed in the TPA and TQ moieties, respectively (Fig. S8A, ESI†). Meanwhile, the spin–orbit coupling (SOC, 0.65 cm^{-1}) was high enough to elicit a more efficient intersystem crossing process. Moreover, the energy gap between T_1 and S_0 is only 0.21 eV, which is inadequate to provide the energy required for oxygen to be excited to $^{1}O_2$ species (0.95 eV). Meanwhile, the TQ-TPA$^{\bullet}$ in the T_1 state could easily obtain an electron from adjacent substances to produce TQ-TPA$^{\bullet-}$, from which the electron could transfer to the surrounding tissue to eventually generate $^{\bullet}$OH species (Fig. S8B, ESI†). Therefore, all of the above results indicated that we have obtained NIR II-emitting type I AIE PSs.

3.2. Synthesis and characterization of 2TPE-Gd

Meanwhile, we combined TPE with a Gd complex to explore their interaction with DSPE-PEG. As shown in Scheme S1 (ESI†), the bromomethyl group connected to TPE was allowed to react with tri-*tert*-butyl-2,2′,2″-(10-(2-((2-aminoethyl)amino)-2-oxoethyl)-1,4,7,10-tetraazacyclododecane-1,4,7-triyl)triacetate (DOTA*t*Bu-NH$_2$) at a molar ratio of 2 : 1. After deprotection of the ester groups using trifluoroacetic acid, gadolinium ions were chelated to produce the probe 2TPE-Gd, which was structurally confirmed by NMR spectral characterization (Fig. S9 and S10, ESI†). Its absorption (Fig. S11A, ESI†) and emission peaks in THF (Fig. S11B, ESI†) were recorded at 320 and 470 nm, respectively. The PL spectral measurement in THF/water mixtures with different f_w indicated that 2TPE-Gd is also AIE active (Fig. S11B and S11C, ESI†). In addition, 2TPE-Gd had a low critical micelle concentration (CMC) of 4.9 μM (Fig. S12A and B, ESI†), suggesting that it could easily form micelles in aqueous solution. These properties facilitated its interaction with DSPE-PEG for exploring the effect on relaxivity. In water, 2TPE-Gd gave strong blue emission because of the formation of aggregates. However, its PL intensity gradually decreased upon addition of DSPE-PEG due to de-aggregation of the molecules (Fig. 2F), and the trade-off value was recorded as the weight ratio of 16 : 1 DSPE-PEG/2TPE-Gd (Fig. 2G and Fig. S13, ESI†). Interestingly, the relaxation rate gradually increased with increasing DSPE-PEG and also reached the maximum at the weight ratio of 16 : 1 (Fig. 2H). The reason might be that with the increase in DSPE-PEG, the 2TPE-Gd aggregates were de-aggregated by DSPE-PEG to gradually form larger-sized micelles, which could prolong the τ_R of these micelles. Meanwhile, PEGs could hold enough water molecules to prolong the diffusion correlation time (τ_D) of these water molecules, which increased the exchange rate of gadolinium with water protons.[28] All these factors contributed to the improvement of r_1. Furthermore, with the increase of DSPE-PEG, the encapsulation efficiency of 2TPE-Gd also increased, finally reaching more than 85% (Fig. S14, ESI†). Therefore, we used this ratio in the construction of the micelles.

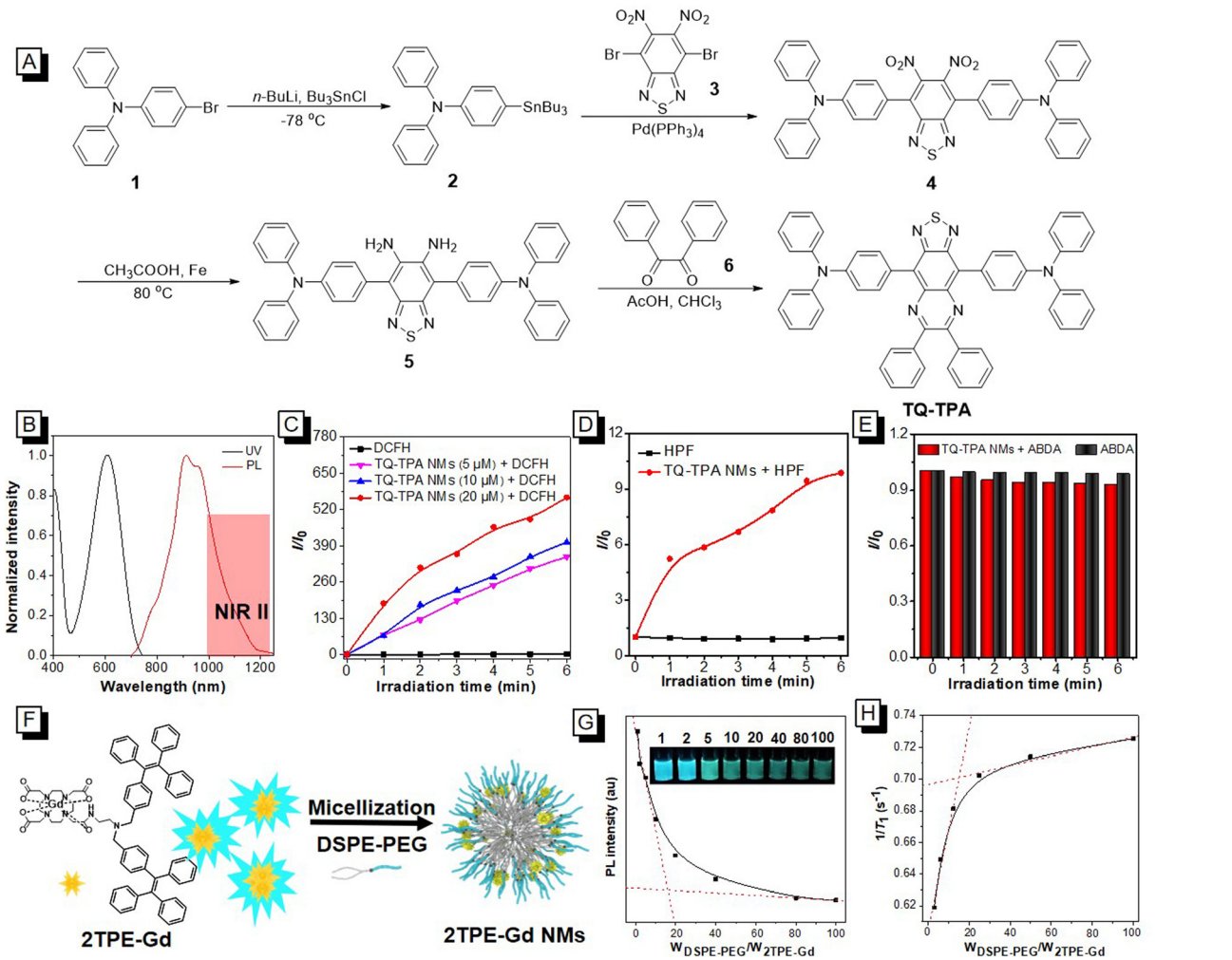

Fig. 2 The synthesis and property characterization of TQ-TPA and 2TPE-Gd. (A) The synthetic route of TQ-TPA. (B) The absorption and PL spectra of TQ-TPA in THF solution (10 μM). (C) ROS generation of different concentrations (5, 10, and 20 μM) of TQ-TPA NMs under 660 nm laser irradiation (0.3 W cm^{-2}) using DCFH as an indicator. (D) Plots of relative PL intensity of HPF (for •OH detection) with or without TQ-TPA NMs (10 μM) under 660 nm laser irradiation (0.3 W cm^{-2}). (E) The decomposition rates of ABDA (100 μM) with or without TQ-TPA NMs (10 μM) under 660 nm laser irradiation (0.3 W cm^{-2}). (F) Schematic illustration of aggregation of 2TPE-Gd with strong fluorescence in water and de-aggregation of 2TPE-Gd by the insertion of DSPE-PEG to form 2TPE-Gd nanomicelles, leading to a decrease in fluorescence intensity. (G) PL intensity of 2TPE-Gd (10 μM) upon addition of different weights of DSPE-PEG. The inset shows the fluorescence images at different weight ratios of DSPE-PEG/2TPE-Gd. (H) The relaxation rate of different weight ratios of DSPE-PEG/2TPE-Gd with a certain concentration (50 μM) of 2TPE-Gd.

3.3. Construction and characterization of TGdTT NMs

After successfully obtaining the AIE type I PS and amphiphilic AIE-Gd, we constructed TGdTT NMs by self-assembly of TQ-TPA/DSPE-PEG/2TPE-Gd with the feeding weight ratio of 16 : 16 : 1 (Fig. 3A). The transmission electron microscopy (TEM) analysis showed that TGdTT NMs had a spherical morphology with a size of 52.2 ± 10.2 nm, which was consistent with the result from dynamic light scattering (DLS) of 91.3 ± 3.9 nm (Fig. 3B). Compared with the TGdTT NMs, the morphology of the 2TPE-Gd NMs (Fig. S15, ESI†) was irregular, with a size of around 37 nm, which indicated that the addition of TQ-TPA molecules significantly increased the size of the nanomicelles. Notably, the TGdTT NMs were stable in phosphate buffered saline (PBS) for more than 15 days (Fig. S16, ESI†). The absorption and PL spectra of the TGdTT NMs were similar to those of the TQ-TPA NMs (Fig. 3C). Moreover, the PL quantum yield of the TGdTT NMs (~3%, Fig. S17A, ESI†) was almost same as that of the TQ-TPA NMs (Fig. S17B, ESI†), indicating that the introduction of 2TPE-Gd did not interfere with the emission properties of TQ-TPA. Subsequently, we compared the ROS generation ability of the TGdTT NMs, TQ-TPA NMs, and chlorin e6 (Ce6). The results showed that the fluorescence intensity of DCF in an aqueous solution of TGdTT NMs was slightly lower than that in an aqueous solution of TQ-TPA NMs, but was still much higher than that of Ce6 under the same experimental conditions (Fig. S18, ESI†). The reason for this might be that the gadolinium complex quenched the emission of the DCF indicator to some extent due to the ACQ property of the DCF molecules.

We next evaluated the r_1 values of the TGdTT NMs, 2TPE-Gd NMs, 2TPE-Gd, and clinical MRI CA Gd-DOTA in a 0.5 T MRI

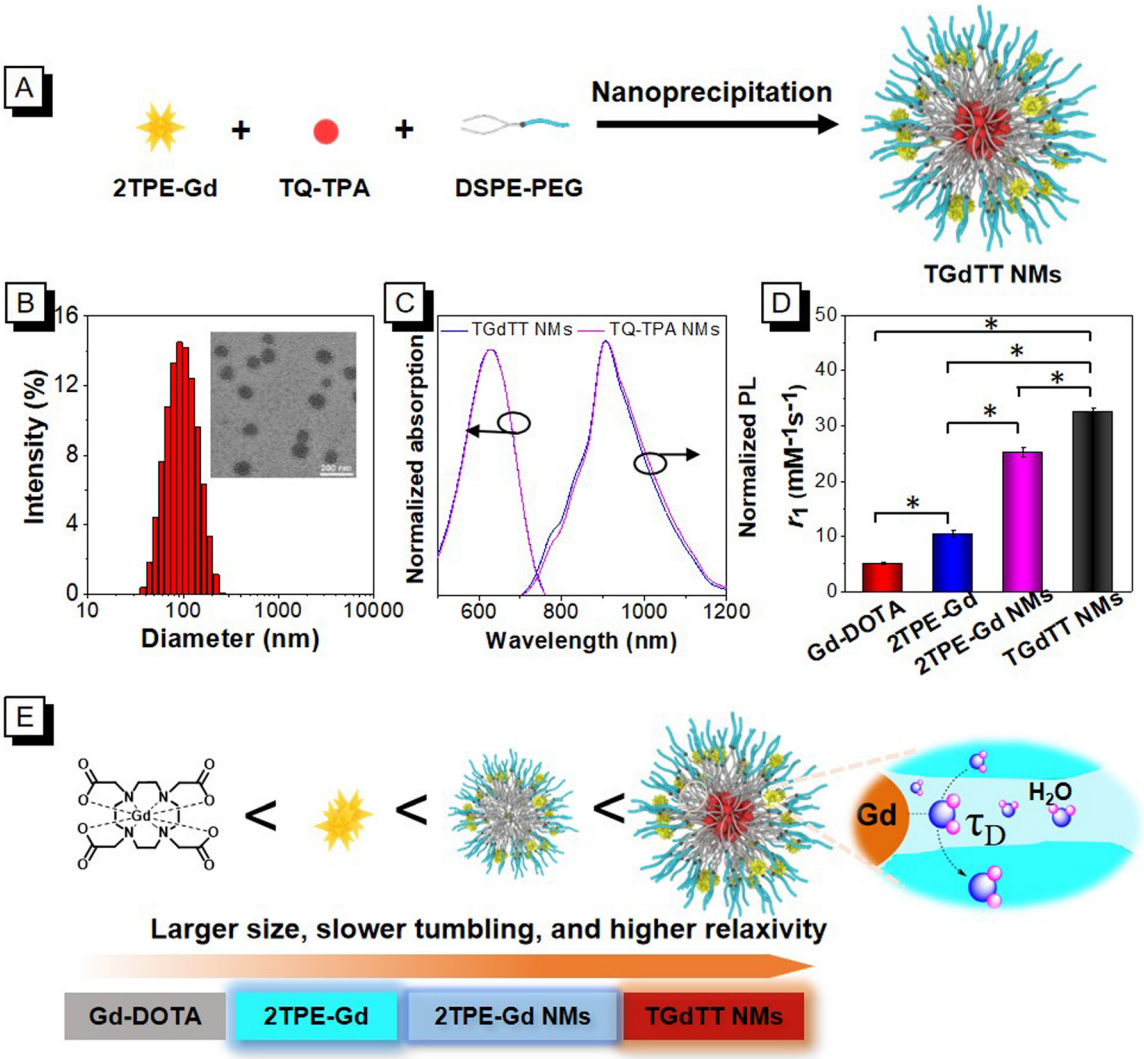

Fig. 3 Construction and characterization of TGdTT NMs. (A) Construction procedure of TGdTT NMs. (B) DLS results of TGdTT NMs. The inset is the TEM image of the TGdTT NMs. (C) Normalized absorption and PL spectra of TGdTT NMs and TQ-TPA NMs in aqueous solution. (D) Relaxivities of TGdTT NMs, 2TPE-Gd NMs, 2TPE-Gd, and Gd-DOTA at 0.5 T (n = 3). Data are reported as mean ± SD and analyzed using one-way ANOVA followed by LSD test. *P < 0.001. (E) Illustration of the mechanism of enhancement of relaxivity from 2TPE-Gd to TGdTT NMs.

scanner. As shown in Fig. 3D and listed in Table S1 (ESI†), the relaxivity of the TGdTT NMs was recorded as 32.5 ± 0.6 mM^{-1} s^{-1}, which was not only higher than that of the 2TPE-Gd NMs (25.3 ± 0.8 mM^{-1} s^{-1}), but also 3 and 6 times larger than those of 2TPE-Gd (10.5 ± 0.6 mM^{-1} s^{-1}) and Gd-DOTA (5.2 ± 0.2 mM^{-1} s^{-1}). This could be ascribed to the larger size of the nanomicelles attenuating the rotation of 2TPE-Gd and diffusion of water molecules trapped in the DSPE-PEG chains compared with 2TPE-Gd and Gd-DOTA, which could be identified from the hydration diameters of the TGdTT NMs (91.3 ± 3.9 nm), 2TPE-Gd NMs (78.8 ± 5.4 nm), 2TPE-Gd (5.6 ± 0.4 nm), and Gd-DOTA (0.8 ± 0.03 nm) (Fig. 3E and Table S1, ESI†). Thus, all of above results indicated that TGdTT NMs would be a very attractive platform integrating NIR II emission, high MR contrast, and efficient type I ROS generation ability for biological applications.

3.4. Bimodal *in vitro* NIR II FL/MRI and cell killing with TGdTT NMs

Subsequently, we explored the applications of the NMs in cancer-cell imaging and killing. First, the biocompatibility of the TGdTT NMs was evaluated *via* tetrazolium-based colorimetric assays, and the results suggested that the TGdTT NMs had good biocompatibility even at a high Gd(III) concentration of 50 μM (Fig. S19, ESI†). Confocal laser scanning microscopy (CLSM) analysis revealed that the TGdTT NMs could light up cells, and were mainly located in the lysosomes, which was confirmed by cell co-localization experiments (Fig. 4A and Fig. S20, ESI†). Furthermore, the T_1-weighted phantom images in the *in vitro* experimental results demonstrated that the TGdTT NMs showed a stronger contrast signal than that of Gd-DOTA at 0.5 T (Fig. 4B and Fig. 4C). Notably, inductively coupled plasma mass spectrometry (ICP-MS) showed that the

amounts of TGdTT NM and Gd-DOTA uptake by cells were 117.78 ± 2.98 and 118.22 ± 5.24 fg Gd(III) per cell. These results demonstrated that the TGdTT NMs had better T_1-weighted contrast ability than Gd-DOTA at the same Gd(III) concentration *in vitro*.

To evaluate the ROS generation ability of the TGdTT NMs at the cell level, 2′,7′-dichlorodihydrofluorescein diacetate (DCFH-DA) was chosen as an indicator; this can more easily permeate the cell membrane than hydrolyzed DCFH and be deacetylated to DCFH by intracellular esterase, allowing detection of ROS. As shown in Fig. S21 (ESI†), the 4T1 cancer cells showed bright green emission in the TGdTT NM group under laser irradiation. Meanwhile, there was no emission observed in the cells with only TGdTT NMs or only laser irradiation, or in the PBS group (blank). Because of the superb type I ROS generation ability, the cell viability obviously decreased with increasing concentration of TGdTT NMs under 660 nm laser irradiation for 5 min (Fig. 4D). The calcein AM/propidium iodide experiments suggested that the TGdTT NMs with photo-irradiation demonstrated efficient cancer-cell killing ability (Fig. 4E).

3.5. Bimodal MR/NIR II FLI of TGdTT NMs *in vivo* and pharmacokinetic evaluation

Besides evaluation at the cell level, the TGdTT NMs were also applied in subcutaneous 4T1 tumor-bearing mice to show their dual-modal imaging and therapy. Based on the excellent T_1-weighted contrast ability of the TGdTT NMs, we first explored the MRI of tumor-bearing female Balb/c mice using a 9.4 T MRI scanner, and clinical MRI CA Gd-DOTA was used as a control. After intravenous injection of TGdTT NMs, T_1-weighted MR images were collected at different times. As shown in Fig. 5A, remarkable T_1-weighted contrast signals were observed in the tumor region, and the signal strength of the tumor reached a maximum at 7 h post-injection. In comparison, due to the low r_1 and rapid renal clearance, weak contrast signals could be observed in the Gd-DOTA group with the same dose of Gd(III), which was also confirmed by the relative contrast-to-noise ratio (CNR_{post}/CNR_{pre}).[15] At 7 h post-injection, the CNR_{post}/CNR_{pre} of the TGdTT NM group was 12 times higher than that of the Gd-DOTA group (Fig. 5B), demonstrative of the excellent imaging performance of the T NMs. These results confirmed that TGdTT NMs could enhance the T_1-weighted tumor contrast and permit long-term MRI imaging of tumors.

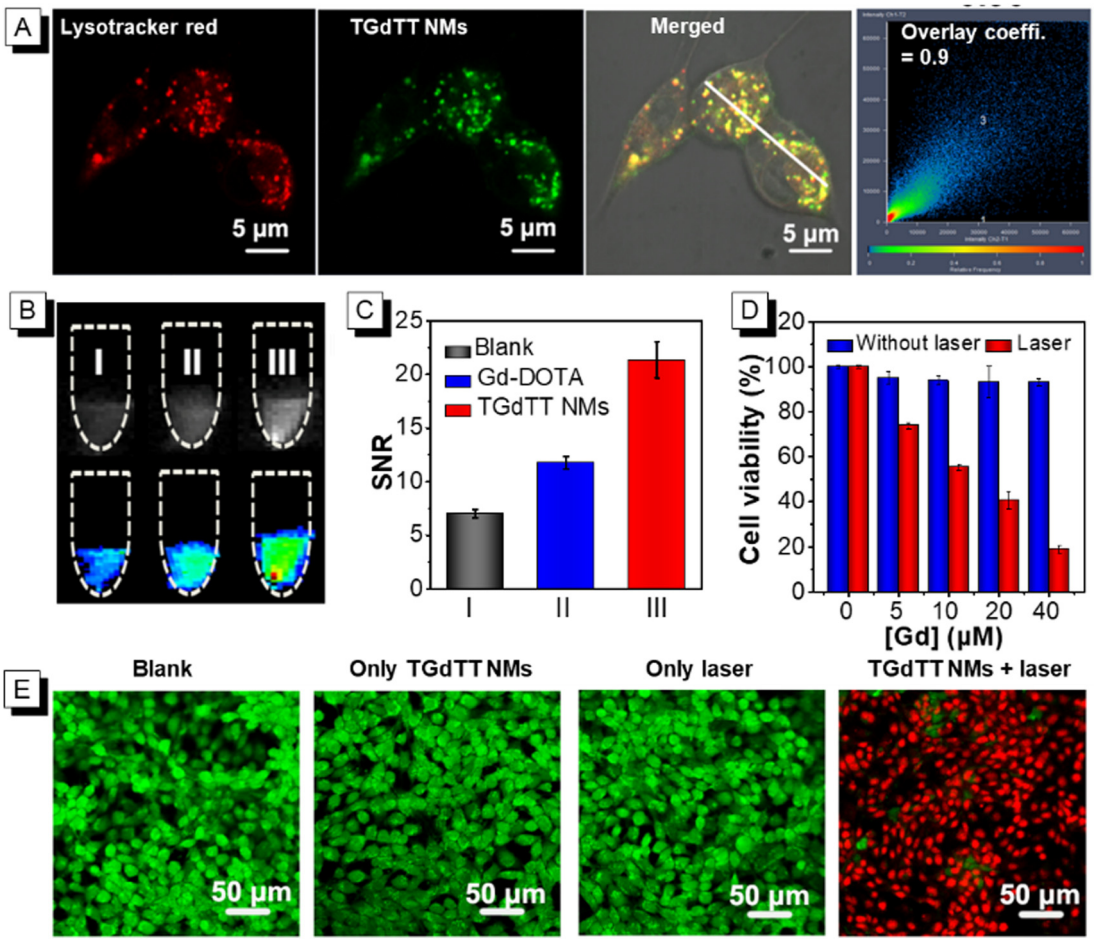

Fig. 4 Cell imaging and *in vitro* PDT. (A) Co-localization imaging of TGdTT NMs and LysoTracker™ Red by CLSM. (B) 4T1 cell phantom images of blank (I), Gd-DOTA (II), and TGdTT NMs (III) at 0.5 T. (C) The signal-to-noise ratios (SNRs) of the phantom images in (B). (D) Cell viability with TGdTT NMs by MTT, with or without 660 nm laser irradiation (0.3 W cm^{-2}, 5 min). (E) Dead and live 4T1 cell co-staining assays using propidium iodide (red, dead cell) and calcein-AM (green, live cell) as fluorescence probes.

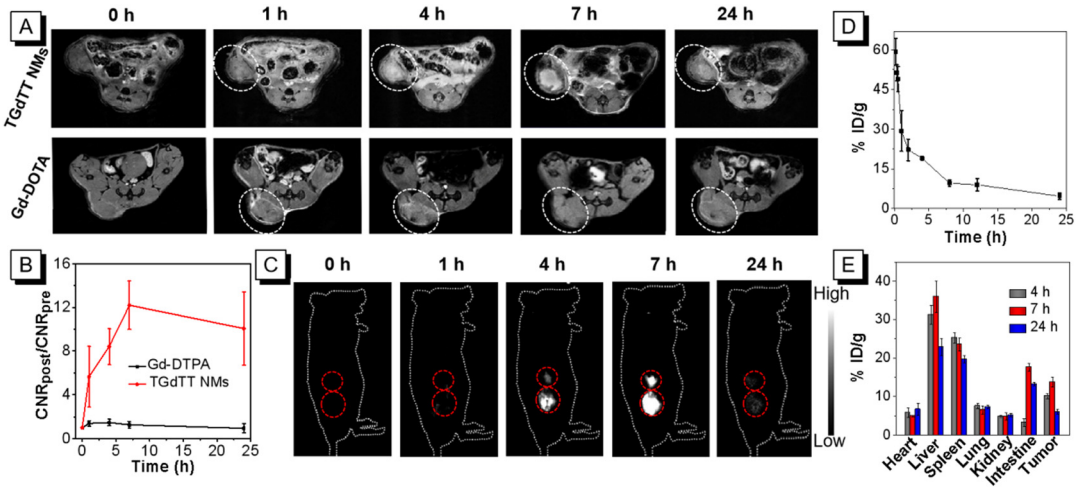

Fig. 5 Dual-modal *in vivo* MRI/NIR II FLI. (A) MRI of 4T1 tumor-bearing mice at 0, 1, 4, 7, and 24 h after intravenous injection of TGdTT NMs (0.5 g TGdTT NMs per kg body weight). The white dashed circles indicate the tumor. (B) CNR_{post}/CNR_{pre} of MRI tumor signals at different times. (C) NIR II FLI of 4T1 tumor-bearing mice at 0, 1, 4, 7, and 24 h after intravenous injection of TGdTT NMs (0.5 g TGdTT NMs per kg body weight). The red dashed circles indicate the tumor. (D) Blood circulation curve of TGdTT NMs in the blood at different times after intravenous injection (n = 3). (E) Tissue distribution of TGdTT NMs in 4T1 tumor-bearing mice at 0, 4, 7, and 24 h after intravenous injection (n = 3 per group).

Taking advantage of the deep penetration depth and high signal-to-noise ratio of NIR II FLI, we subsequently used the TGdTT NMs in NIR II FLI to validate their accumulation at tumor sites. As shown in Fig. 5C and Fig. S22 (ESI†), the emission peak was observed at 7 h post-injection, and the fluorescence signal became weak at 24 h post-injection. This result was consistent with that of T_1-weighted MRI. Based on the high tissue penetration depth and spatial resolution of MRI and excellent sensitivity and signal-to-noise ratio of FLI, the tumor site and geometry could be delineated comprehensively, being beneficial for tumor therapy. These results unambiguously demonstrated that the TGdTT NMs are excellent MRI/NIR II FLI dual-modal probes for tumor imaging, and could precisely locate tumor sites and further guide PDT.

To further evaluate the uptake of the TGdTT NMs by tumors *in vivo*, the blood circulation and bio-distribution of the TGdTT NMs were studied by measuring Gd(III) concentrations in the blood and tissues at different times. The blood-circulation curve showed that there was a steady-state period from 0.5 to 4 h (Fig. 5D), which provided the TGdTT NMs with enough time to circulate in the body and accumulate in the tumor through the enhanced permeability and retention (EPR) effect.[37] The bio-distribution study suggested that they mainly accumulated in the liver, spleen, intestine, and tumor (Fig. 5E). This result suggests that they were mainly held in the liver and spleen by the reticuloendothelial system and excreted through the hepatobiliary route.[38,39]

3.6. PDT for tumor inhibition and biosafety evaluation

Under the guidance of dual-modal MR/NIR II FL imaging, the ablation ability towards a subcutaneous tumor by 660 nm light-induced PDT was explored. After intravenous injection of the TGdTT NMs for 7 h, 4T1 tumor-bearing female mice were irradiated for 10 min. During the treatment, the injection and laser irradiation were carried out every four days as shown in Fig. 6A, and the tumor volume and body weight were measured every two days. After treating three times, tumor sections stained with hematoxylin and eosin (H&E) showed that the group treated with TGdTT NMs and laser irradiation had sparse nuclei compared with the dense cancer-cell nuclei of the control groups treated with only TGdTT NMs, only laser irradiation, or PBS (Fig. 6B), indicating that most of the cancer cells had been killed. In addition, the relative tumor volume of the control groups obviously increased by 8 ~ 12 times. In sharp contrast, the tumor growth in the group treated with TGdTT NMs and laser irradiation was greatly inhibited (Fig. 6C and Fig. S23, ESI†). These results verified that the TGdTT NMs could generate enough type I ROS upon photo-irradiation to inhibit tumor growth. Notably, during the treatment period, the mouse weights in the four groups showed a similar growth trend (Fig. 6D), suggesting that there were no detectable side effects of these treatments for the mice.

To evaluate the biosafety of TGdTT NMs, they were intravenously injected into healthy female BALB/c mice, and PBS was used as the control. After 30 days, these mice were sacrificed and their blood and major tissues were collected to evaluate the biosafety. The H&E staining of major organs revealed that histologically no cell necrosis or inflammation occurred (Fig. S24, ESI†). In addition, the indices of liver and renal function tests showed no noticeable abnormalities (Fig. S25, ESI†). All of these results demonstrated that TGdTT NMs show excellent biocompatibility for theranostic applications.

4. Conclusion

In this work, a novel strategy based on aggregation and de-aggregation of two AIEgens for the construction of TGdTT NMs with dual-modal MRI/NIR II FLI and PDT effects was presented.

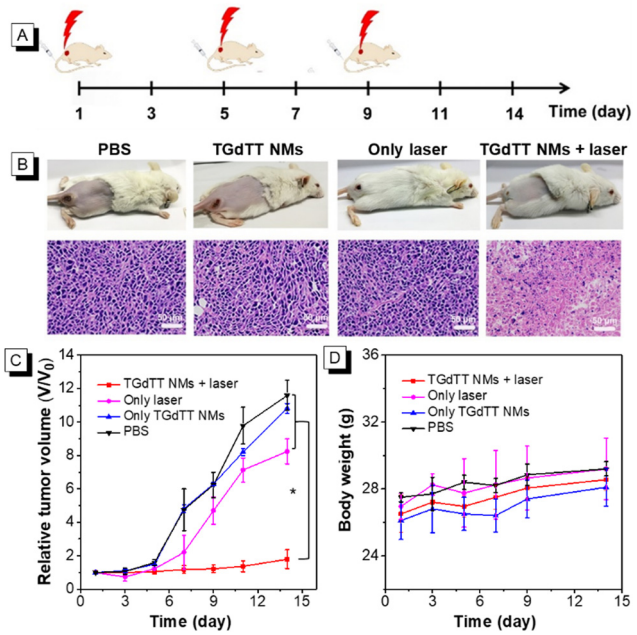

Fig. 6 *In vivo* efficacy of TGdTT-mediated PDT. (A) *In vivo* treatment timeline. (B) Representative digital photographs and H&E staining of tumor slices of mice treated with PBS, only TGdTT NMs, only laser irradiation, and TGdTT NMs with laser irradiation after treatment. (C and D) Tumor growth curves and body weight changes of mice after various treatments (n = 3 per group). Error bars indicate standard deviations of means. *$P < 0.001$.

The TGdTT NMs were formed by the aggregation of hydrophobic TQ-TPA in their core and de-aggregation of amphipathic 2TPE-Gd in the interface of the DSPE-PEG nanomicelles. Notably, the r_1 of the Gd(III) complexes in the TGdTT NMs increased significantly because of the attenuation of the rotation of 2TPE-Gd due to the large size of the NMs and water trapped in the DSPE-PEG chains. Moreover, excellent NIR II emission and type I ROS generation have also been achieved for the TGdTT NMs owing to the contained TQ-TPA molecules. Because of their enhanced r_1, high ROS generation ability, excellent biocompatibility and biosafety, as well as relatively long blood circulation time to passively target to tumors, the TGdTT NMs realized dual-modal MRI/NIR II FLI-guided PDT, which greatly inhibited tumor growth. Thus, this work provides a new strategy to construct multifunctional nanomaterials based on AIEgens for improved theranostic applications.

Conflicts of interest

There are no conflicts to declare.

Acknowledgements

This work was financially supported by the National Natural Science Foundation of China (21788102, 52103168, and 82172081), the National Key Research and Development Program of China (Intergovernmental cooperation project, 2017YFE0132200), the Natural Science Foundation of Guangdong Province (2019B030301003, 2019A1515012144, and 2016A030312002), the Innovation and Technology Commission of Hong Kong (ITC-CNERC14SC01) and the Independent Research Project of the State Key Lab of Luminescent Materials and Devices (SCUT) (Skllmd-2022-10).

References

1 D. E. Lee, H. Koo, I. C. Sun, J. H. Ryu, K. Kim and I. C. Kwon, Multifunctional nanoparticles for multimodal imaging and theragnosis, *Chem. Soc. Rev.*, 2012, **41**, 2656–2672.
2 D. S. Karaman, M. P. Sarparanta, J. M. Rosenholm and A. J. Airaksinen, Multimodality imaging of silica and silicon materials *in vivo*, *Adv. Mater.*, 2018, **30**, 1703651.
3 B. Qiao, Y. Luo, H. B. Cheng, J. Ren, J. Cao, C. Yang, B. Liang, A. Yang, X. Yuan, J. Li, L. Deng, P. Li, H. T. Ran, L. Hao, Z. Zhou, M. Li, Y. Zhang, P. S. Timashev, X. J. Liang and Z. Wang, Artificial nanotargeted cells with stable photothermal performance for multimodal imaging-guided tumor-specific therapy, *ACS Nano*, 2020, **14**, 12652–12667.
4 L. Zhu, Y. Li, M. Jiang, C. Ke, H. Long, M. Qiu, L. Zhang, C. Ye, X. Zhou, Z. X. Jiang and S. Chen, Self-assembly of precisely fluorinated albumin for dual imaging-guided synergistic chemo-photothermal-photodynamic cancer therapy, *ACS Appl. Mater. Interfaces*, 2023, **15**, 2665–2678.
5 H. Li, Y. Liu, B. Huang, C. Zhang, Z. Wang, W. She, Y. Liu and P. Jiang, Highly efficient GSH-responsive "off–on" NIR-II fluorescent Fenton nanocatalyst for multimodal imaging-guided photothermal/chemodynamic synergistic cancer therapy, *Anal. Chem.*, 2022, **94**, 10470–10478.
6 Q. Yang, Z. Ma, H. Wang, B. Zhou, S. Zhu, Y. Zhong, J. Wang, H. Wan, A. Antaris, R. Ma, X. Zhang, J. Yang, X. Zhang, H. Sun, W. Liu, Y. Liang and H. Dai, Rational design of molecular fluorophores for biological imaging in the NIR-II window, *Adv. Mater.*, 2017, **29**, 1605497.
7 S. Zhu, Q. Yang, A. L. Antaris, J. Yue, Z. Ma, H. Wang, W. Huang, H. Wan, J. Wang, S. Diao, B. Zhang, X. Li, Y. Zhong, K. Yu, G. Hong, J. Luo, Y. Liang and H. Dai, Molecular imaging of biological systems with a clickable dye in the broad 800 to 1700 nm near-infrared window, *Proc. Natl. Acad. Sci. U. S. A.*, 2017, **114**, 962–967.
8 L. Lu, B. Li, S. Ding, Y. Fan, S. Wang, C. Sun, M. Zhao, C. X. Zhao and F. Zhang, NIR-II bioluminescence for *in vivo* high contrast imaging and in situ ATP-mediated metastases tracing, *Nat. Commun.*, 2020, **11**, 4192.
9 J. Qi, N. Alifu, A. Zebibula, P. Wei, J. W. Y. Lam, H.-Q. Peng, R. T. K. Kwok, J. Qian and B. Z. Tang, Highly stable and bright AIE dots for NIR-II deciphering of living rats, *Nano Today*, 2020, **34**, 100893.
10 Z. Ma, F. Wang, W. Wang, Y. Zhong and H. Dai, Deep learning for *in vivo* near-infrared imaging, *Proc. Natl. Acad. Sci. U. S. A.*, 2021, **118**, e2021446118.
11 M. H. Lee, E. J. Kim, H. Lee, H. M. Kim, M. J. Chang, S. Y. Park, K. S. Hong, J. S. Kim and J. L. Sessler, Liposomal Texaphyrin Theranostics for Metastatic Liver Cancer, *J. Am. Chem. Soc.*, 2016, **138**, 16380–16387.

12 H. Li, G. Parigi, C. Luchinat and T. J. Meade, Bimodal fluorescence-magnetic resonance contrast agent for apoptosis imaging, *J. Am. Chem. Soc.*, 2019, **141**, 6224–6233.
13 R. Yan, Y. Hu, F. Liu, S. Wei, D. Fang, A. J. Shuhendler, H. Liu, H. Y. Chen and D. Ye, Activatable NIR fluorescence/MRI bimodal probes for *in vivo* imaging by enzyme-mediated fluorogenic reaction and self-assembly, *J. Am. Chem. Soc.*, 2019, **141**, 10331–10341.
14 H. Li, D. Luo, C. Yuan, X. Wang, J. Wang, J. P. Basilion and T. J. Meade, Magnetic resonance imaging of PSMA-positive prostate cancer by a targeted and activatable Gd(III) MR contrast agent, *J. Am. Chem. Soc.*, 2021, **143**, 17097–17108.
15 V. S. Harrison, C. E. Carney, K. W. MacRenaris, E. A. Waters and T. J. Meade, Multimeric near IR-MR contrast agent for multimodal *in vivo* imaging, *J. Am. Chem. Soc.*, 2015, **137**, 9108–9116.
16 H. Li, H. Kim, J. Han, V. N. Nguyen, X. Peng and J. Yoon, Activity-based smart AIEgens for detection, bioimaging, and therapeutics: recent progress and outlook, *Aggregate*, 2021, **2**, e51.
17 Y. L. Balachandran and X. Jiang, Aggregation-induced fluorogens in bio-detection, tumor imaging, and therapy: a review, *CCS Chem.*, 2022, **4**, 420–436.
18 Z. Zhang, M. Kang, H. Tan, N. Song, M. Li, P. Xiao, D. Yan, L. Zhang, D. Wang and B. Z. Tang, The fast-growing field of photo-driven theranostics based on aggregation-induced emission, *Chem. Soc. Rev.*, 2022, **51**, 1983–2030.
19 T. Zhou, R. Hu, L. Wang, Y. Qiu, G. Zhang, Q. Deng, H. Zhang, P. Yin, B. Situ, C. Zhan, A. Qin and B. Z. Tang, An AIE-active conjugated polymer with high ROS-generation ability and biocompatibility for efficient photodynamic therapy of bacterial infections, *Angew. Chem., Int. Ed.*, 2020, **59**, 9952–9956.
20 Z. Zhuang, J. Dai, M. Yu, J. Li, P. Shen, R. Hu, X. Lou, Z. Zhao and B. Z. Tang, Type I photosensitizers based on phosphindole oxide for photodynamic therapy: apoptosis and autophagy induced by endoplasmic reticulum stress, *Chem. Sci.*, 2020, **11**, 3405–3417.
21 D. Chen, Q. Xu, W. Wang, J. Shao, W. Huang and X. Dong, Type I photosensitizers revitalizing photodynamic oncotherapy, *Small*, 2021, **17**, 2006742.
22 M. Kang, Z. Zhang, W. Xu, H. Wen, W. Zhu, Q. Wu, H. Wu, J. Gong, Z. Wang, D. Wang and B. Z. Tang, Good steel used in the blade: well-tailored Type-I photosensitizers with aggregation-induced emission characteristics for precise nuclear targeting photodynamic therapy, *Adv. Sci.*, 2021, **8**, 2100524.
23 Q. Sun, Q. Su, Y. Gao, K. Zhou, W. Song, P. Quan, X. Yang, Z. Ge, Y. Zhang and G. He, Cationic telluroviologen derivatives as Type-I photosensitizers for tumor photodynamic theranostics, *Aggregate*, 2022, e298.
24 T. C. Pham, V.-N. Nguyen, Y. Choi, S. Lee and J. Yoon, Recent strategies to develop innovative photosensitizers for enhanced photodynamic therapy, *Chem. Rev.*, 2021, **121**, 13454–13619.
25 J. Hu and S. Liu, Recent advances on stimuli-responsive macromolecular magnetic resonance imaging (MRI)contrast agents, *Sci. China: Chem.*, 2018, **61**, 1110–1122.
26 J. Wahsner and E. M. Gale, A. Rodriguez-Rodriguez, P. Caravan, Chemistry of MRI contrast agents: current challenges and new frontiers, *Chem. Rev.*, 2019, **119**, 957–1057.
27 Y. Chen, M. Li, Y. Hong, J. W. Lam, Q. Zheng and B. Z. Tang, Dual-modal MRI contrast agent with aggregation-induced emission characteristic for liver specific imaging with long circulation lifetime, *ACS Appl. Mater. Interfaces*, 2014, **6**, 10783–10791.
28 J. S. Ananta, B. Godin, R. Sethi, L. Moriggi, X. Liu, R. E. Serda, R. Krishnamurthy, R. Muthupillai, R. D. Bolskar, L. Helm, M. Ferrari, L. J. Wilson and P. Decuzzi, Geometrical confinement of gadolinium-based contrast agents in nanoporous particles enhances T_1 contrast, *Nat. Nanotechnol.*, 2010, **5**, 815–821.
29 A. G. Robertson and L. M. Rendina, Gadolinium theranostics for the diagnosis and treatment of cancer, *Chem. Soc. Rev.*, 2021, **50**, 4231–4244.
30 L. Wang, Q. Wan, R. Zhang, B. Situ, K. Ni, J. Gao, X. Feng, P. Zhang, Z. Wang, A. Qin and B. Z. Tang, Synergistic enhancement of fluorescence and magnetic resonance signals assisted by albumin aggregate for dual-modal imaging, *ACS Nano*, 2021, **15**, 9924–9934.
31 C. Zhu, S. Pang, J. Xu, L. Jia, F. Xu, J. Mei, A. Qin, J. Sun, J. Ji and B. Z. Tang, Aggregation-induced emission of tetraphenylethene derivative as a fluorescence method for probing the assembling/disassembling of amphiphilic molecules, *Analyst*, 2011, **136**, 3343–3348.
32 A. Bose, D. Roy Burman, B. Sikdar and P. Patra, Nanomicelles: types, properties and applications in drug delivery, *IET Nanobiotechnol.*, 2021, **15**, 19–27.
33 H. Gong, Z. Dong, Y. Liu, S. Yin, L. Cheng, W. Xi, J. Xiang, K. Liu, Y. Li and Z. Liu, Engineering of multifunctional nano-micelles for combined photothermal and photodynamic therapy under the guidance of multimodal imaging, *Adv. Funct. Mater.*, 2014, **24**, 6492–6502.
34 H. Cao, Y. Yang and J. Li, AIEgen-lipid structures: assembly and biological applications, *Aggregate*, 2020, **1**, 69–79.
35 L. Wang, H. Lin, X. Chi, C. Sun, J. Huang, X. Tang, H. Chen, X. Luo, Z. Yin and J. Gao, A self-assembled biocompatible nanoplatform for multimodal MR/fluorescence imaging assisted photothermal therapy and prognosis analysis, *Small*, 2018, **14**, 1801612.
36 B. Lu, Y. Huang, Z. Zhang, H. Quan and Y. Yao, Organic conjugated small molecules with donor-acceptor structures: design and application in the phototherapy of tumors, *Mater. Chem. Front.*, 2022, **6**, 2968–2993.
37 A. Nel, E. Ruoslahti and H. Meng, New insights into ''permeability'' as in the enhanced permeability and retention effect of cancer nanotherapeutics, *ACS Nano*, 2017, **11**, 9567–9569.
38 K. Yang, J. Wan, S. Zhang, Y. Zhang, S. T. Lee and Z. Liu, *In vivo* pharmacokinetics, long-term biodistribution, and toxicology of PEGylated graphene in mice, *ACS Nano*, 2011, **5**, 516–522.
39 N. Sharma, M. A. Saifi, S. B. Singh and C. Godugu, *In vivo* studies: toxicity and biodistribution of nanocarriers in organisms, in *Nanotoxicity*, Elsevier, 2020, ch. 3, pp. 41–70.